atically enumerating nets of this type. Nets 61 and 64 (Fig. 8) provide a nice example of a pair of nets with the same space group and unit-cell dimensions.

In some of these nets, the skew quadrangles approach regular tetrahedra; if the tetrahedra were indeed regular, the nets would become 5-connected and have higher symmetry and higher density. This is perhaps most easily seen for net 60 (Fig. 7). With regular tetrahedra, the symmetry would be $P4_2/mmc$ with $a = 2, c = 2 + 2^{1/2}$ and vertices in 8 (o) 0, y, z with $y = 1/4$ and $z = 0.1465$. The density is 3% higher. In the conformation listed in Table 2, however, the next shortest distance (d_2 in Table 2) is ca 20% longer.

References

BOISEN, M. B., GIBBS, G. V. & BUKOWINSKI, M. S. T. (1994). *Phys. Chem. Miner.* **21**, 269–284.
HAN, S. & SMITH, J. V. (1994). *Acta Cryst.* A**50**, 302–307.
HYDE, S. T. (1994). *Acta Cryst.* A**50**, 753–759.
JOHNSTON, R. L. & HOFFMANN, R. (1989). *J. Am. Chem. Soc.* **111**, 810–819.
MEIER, W. M. & OLSON, D. H. (1992). *Atlas of Zeolite Structure Types*, International Zeolite Association Special Publication, 3rd revised ed. London: Butterworths-Heinemann.
O'KEEFFE, M. (1991). *Z. Kristallogr.* **196**, 21–37.
O'KEEFFE, M. (1992). *Acta Cryst.* A**48**, 670–673.
O'KEEFFE, M. (1995). *Phys. Chem. Miner.* In the press.
O'KEEFFE, M. & BRESE, N. E. (1992). *Acta Cryst.* A**48**, 663–669.
PARISE, J. B. (1980). *Acta Cryst.* B**36**, 1179–1180.
SMITH, J. V. (1978). *Am. Mineral.* **63**, 960–969.
SMITH, J. V. & BENNETT, J. M. (1981). *Am. Mineral.* **66**, 777–788.
TROJER, F. J. (1966). *Am. Mineral.* **51**, 890–894.
ZACHARIASEN, W. H. (1963). *Acta Cryst.* **16**, 380–384.

Dynamical Approach for X-ray Diffraction from Surfaces and Interfaces: Interpretation of Crystal Truncation Rod Using Dynamical Theory

BY TSAI-SHENG GAU AND SHIH-LIN CHANG

Department of Physics, National Tsing Hua University and Synchrotron Radiation Research Center, Hsinchu, Taiwan 30043

Abstract

X-ray diffraction from crystal surfaces and interfaces is described within the framework of the dynamical theory. The intensity distributions of specular and non-specular crystal truncation rods are interpreted with this dynamical approach. Difficulties encountered in the ordinary dynamical calculation for these rods are mentioned and the details of the numerical calculation procedure which overcomes the difficulties are given. The coordinates of dispersion surface, linear absorption coefficients and mode excitations of surface diffractions are calculated and the validity of this dynamical approach is discussed.

1. Introduction

Grazing-incidence X-ray diffraction (GIXD) from crystal surfaces and interfaces has been widely used for determining surface crystal structures since 1979 (Marra, Eisenberger & Cho, 1979). These include the structures of Si (111) 7 × 7 (Robinson, Waskiewicz, Fuoss, Stark & Johnson, 1986), Ge (111) c 2 × 8 (Feidenhans'l *et al.*, 1988), As/Si (100) (Jedrecy *et al.*, 1990), Pb/Si (111) (Grey, Feidenhans'l, Nielsen & Johnson, 1989) and many others (Robinson & Tweet, 1992; Shimura &

Harada, 1993). Although a crystal surface is a two-dimensional arrangement of atoms, its relative position with respect to the crystal bulk involves the third dimension along the crystal surface normal. To probe this three-dimensional structure, in-plane scan and surface-normal scan are usually employed to gather the structural information parallel and perpendicular to the crystal surface, respectively. The latter, surface-normal scan, is sometimes called crystal-truncation-rod (CTR) scan in the literature (Andrews & Cowley, 1986; Robinson, 1986) because the scan is along the reciprocal rods which are the Fourier transform of a surface-truncated crystal in the reciprocal space (Fig. 1). This CTR scan is also a powerful tool to help solve interface structures on the atomic scale, for example, the structures of NiSi$_2$/Si (111) (Robinson, Tung & Feidenhans'l, 1988), Si/Si (111) (Robinson, Waskiewicz, Tung & Bohr, 1986) and SiO$_2$/Si (111) (Kashiwagura *et al.*, 1987). Aside from the crystal structure determination, GIXD together with *in situ* experimental techniques also provides a means of studying surface order–disorder, melting and roughening transitions (Mochrie, Zehner, Ocko & Gibbs, 1990; Held, Jordan-Sweet, Horn, Mak & Feldman, 1989; Dosch, Mailander, Reichert, Peisl &

Johnson, 1991; Liang, Sirota, D'Amico, Hughes & Sinha, 1987).

Although this well established diffraction technique has succeeded in determining surface/interface structures and explaining surface phenomena, there still seems lacking a rigorous and complete general theory to account for the diffraction intensity measured and the detailed diffraction mechanisms involved in surface X-ray diffraction. In the literature, kinematical theory has frequently been used to interpret experimental findings, where the idea of Born approximation was usually adopted (Vineyard, 1982; Dosch, Batterman & Wack, 1986; Robinson, 1986). This approach suffers, however, from the inability to resolve the following two fundamental problems: (i) the calculated intensity blows up at the exact Bragg diffraction position, and (ii) the kinematical approach does not take the crystal boundary conditions into account so that refraction effects cannot be handled properly. Hence, use of kinematical theory is limited only to analyzing diffraction data off the Bragg peaks. This shortcoming makes it necessary for dynamical theory to solve the problems mentioned, where the boundary conditions and refraction are considered naturally in the theory. In fact, attempts have been made to calculate the intensity distribution of rod scans using dynamical theory (Afanes'ev & Melkonyan, 1983; Colella, 1991; Caticha, 1993), but only limited to either specular rods, where the rods pass through the origin of the reciprocal lattice (see the rod OM in Fig. 1) or a small portion of a non-specular rod (Fig. 1). For a specular rod, diffractions involve no in-plane momentum transfer. Recent reports by Nakatani & Takahashi (1994) and Caticha (1994), utilizing Darwin's treatment, fall into this category. Actually, as depicted in Fig. 1, most CTR rods, displaced from the origin O, are non-specular because the displacement vector, e.g. OG for the rod GL, introduces an in-plane momentum transfer for the incident X-ray beam. Interpretation of the diffraction intensities of these non-specular rods, though difficult, would be more desired since these rods carry structural information in both normal and in-plane directions. Very recently, the dynamical calculation for crystal surface/interface non-specular rods has been briefly reported by Gau & Chang
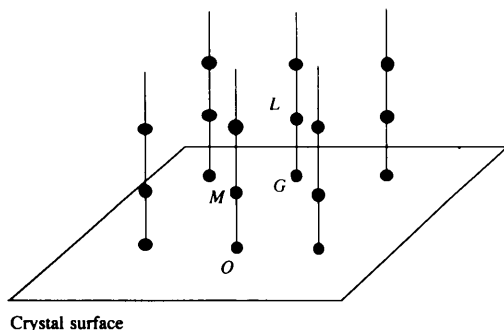
(1994), where a general formalism has been given. However, because the detailed calculation procedure has not been included in that report owing to limited space, some useful dynamical parameters, such as the coordinates of the dispersion surface, linear absorption coefficients and excitation of mode of wave propagation, are not reported. It is the purpose of this paper to present all the details for this general dynamical approach so that the interpretation of surface/interface X-ray diffraction with various geometries can be carried out in a straightforward manner and the diffraction mechanism of GIXD rod scans can be understood in depth.

2. Diffraction geometry and experimental scan schemes

Since a specular rod is a special case of a non-specular rod, for simplicity we consider the non-specular rod GL perpendicular to the crystal surface to start with. Fig. 2 depicts the diffraction geometry in which the relationship is shown among the incident and diffracted wave vectors $\mathbf{k}_i(= \mathbf{CO})$ and $\mathbf{k}_f(= \mathbf{AS})$ outside the crystal and the reciprocal-lattice points O, G and L, where O is the origin and G and L are on the non-specular rod GL. Point A lies on the crystal surface and $\mathbf{CA}$ is perpendicular to the crystal surface. OG, parallel to the crystal surface, is the reciprocal-lattice vector of the atomic planes G and $\mathbf{GS} = \mathbf{q}$ is the momentum transfer along $\mathbf{GL}$. A detector is placed along the $\mathbf{k}_f$ direction. AG and AO are the in-plane components of $\mathbf{k}_i$ and $\mathbf{k}_f$ parallel to the crystal and the angle between the two is φ. $\mathbf{k}_s$ is the wave vector of the surface specularly reflected beam. θ_i and θ_f are the incident and the scattered angles measured from the surface. θ is the angle between the vector $\mathbf{OG}$ and the tangent of the Ewald sphere at point O. During the rod scan along GL, the crystal and the detector are so oriented that θ and φ, namely θ_i and θ_f, are changing. The relationships between θ_i, θ_f and θ, φ according to Feidenhans'l (1989) are

$$\sin^2 \theta_f = \sin^2 \theta_i + 4\cos^2 \theta_i \sin \theta_G (\sin \theta - \sin \theta_G) \quad (1)$$

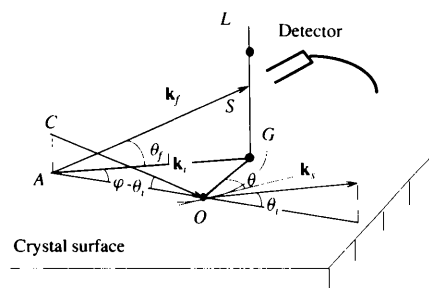$$\sin \varphi = (2\cos \theta \sin \theta_G)/[1 - 4\sin \theta_G(\sin \theta - \sin \theta_G)]^{1/2}, \quad (2)$$

Fig. 1. Crystal truncation rods and reciprocal lattices.

Fig. 2. Geometrical relation between the wave vectors and the crystal surface.

where θ_G is the Bragg angle of the G reflection, which is also equal to $\arcsin[|OG|/2k\cos\theta_i]$ with $k = 1/\lambda$, λ being the X-ray wavelength used. From (2), it is clear that during the rod scan the momentum transfer is varying from OG to OL while keeping the in-plane component always equal to $\mathbf{OG}$. If $\theta_i = \theta_f = 0$, then $\theta = \theta_G$ and $\varphi = 2\theta$. That is, the Bragg condition of the in-plane G reflection is satisfied.

Inside the crystal, the wave vectors $\mathbf{K}_O$, $\mathbf{K}_G$ and $\mathbf{K}_L$ of the incident and diffracted beams are governed by the fundamental equation of the wave field, which will be discussed in the following section.

Experimentally, rod scans can be performed with a four-circle diffractometer or a z-axis diffractometer (Feidenhans'l, 1989), where the z direction is along the crystal-surface normal. When the former is used, both θ_i and θ_f are simultaneously varying during the rod scan. If the latter is employed, θ_i is fixed and only θ_f is varying. These two different scan schemes could lead to different diffraction intensity distributions for the rods.

3. Theoretical consideration

In terms of the dynamical theory of X-ray diffraction, the fundamental equation of the wave field takes the following form:

$$2\varepsilon_M \mathbf{E}_M = \sum_N \chi_{M-N}\mathbf{E}_N \qquad (3)$$

for M and N equal to O, G and L, where $\mathbf{E}_M$ is the electric field of the M-reflected wave and

$$\chi_M = -[e^2\lambda^2/(mc^2\pi V)]F_M, \qquad (4)$$

$$2\varepsilon_M = (K_M^2 - k^2)/k^2, \qquad (5)$$

where m and e are the mass and charge of the electron, V is the volume of the unit cell and F_M is the structure factor of the M reflection. According to the geometric relation, shown in Fig. 3, between the wave vectors $\mathbf{K}_G$ inside the crystal and the directions of the σ- and π-polarized components of each wave, the fundamental equations (3) can be written in matrix form as (Chang, 1984)

deriving (6):

$$\hat{\pi}_O \cdot \hat{\pi}_G = \hat{\pi}_O \cdot \hat{\pi}_L = \cos\varphi',$$
$$\hat{\pi}_O \cdot \hat{\sigma}_L = \sin\alpha\sin\varphi',$$
$$\hat{\sigma}_O \cdot \hat{\sigma}_L = \cos\alpha, \qquad (7)$$
$$\hat{\sigma}_O \cdot \hat{\sigma}_G = 1,$$
$$\hat{\sigma}_O \cdot \hat{\pi}_G = \hat{\sigma}_O \cdot \hat{\pi}_L = \hat{\sigma}_G \cdot \hat{\pi}_O = \hat{\sigma}_G \cdot \hat{\pi}_L = 0,$$

where the angles φ' and α are defined in Fig. 3.

For non-trivial values of E, the determinant of the matrix $\boldsymbol{\Phi}$ must be null, which gives the dispersion relation between the wave vector $\mathbf{K}$ and the related angles θ_i and θ_f:

$$|\boldsymbol{\Phi}| = 0, \qquad (8)$$

from which the coordinates of the tie point C' can be determined. To simplify the derivation, we introduce a variable g, related to the z component of $\mathbf{K}_O$ normal to the surface as $kg = K_{OZ}$. 2ε can then be expressed in terms of g when the tangential components of the wave vectors inside and outside the crystal at the surface boundary are conserved:

$$-2\varepsilon_O = \sin^2\theta_i - g^2,$$
$$-2\varepsilon_G = \sin^2\theta_f - g^2, \qquad (9)$$
$$-2\varepsilon_L = \sin^2\theta_f - g^2 - 4(l/2k - g)(l/2k),$$

where $l = |GL|$. Moreover, the angles α and φ' shown in Fig. 3 can also be expressed as a function of g:

$$\cos\varphi' = (\cos\theta_i\cos\theta_f\cos\varphi + g^2)$$
$$\times [(\cos^2\theta_i + g^2)^{1/2}(\cos^2\theta_f + g^2)^{1/2}]^{-1}, \qquad (10)$$

$$\tan\alpha = l\cos\theta_f/[k\cos^2\theta_f - g(l - kg)]. \qquad (11)$$

The derivation of (10) and (11) is given in Appendix A. By substitution of (9), (10) and (11) into (8), the dispersion relation becomes a twelfth-order non-linear equation of g, which can be solved approximately with iteration procedures, except for some special situations. In practice, the Newton–Ralph method (Press,

$$\Phi E = \begin{pmatrix} \chi_O - 2\varepsilon_O & 0 & \chi_{\bar{G}} & 0 & \chi_{\bar{L}}\cos\alpha & 0 \\ 0 & \chi_O - 2\varepsilon_O & 0 & \chi_{\bar{G}}\cos\varphi' & \chi_{\bar{L}}\sin\alpha\sin\varphi' & \chi_{\bar{L}}\cos\varphi' \\ \chi_G & 0 & \chi_O - 2\varepsilon_G & 0 & \chi_{G-L}\cos\alpha & 0 \\ 0 & \chi_G\cos\varphi' & 0 & \chi - 2\varepsilon_G & 0 & \chi_{G-L} \\ \chi_L\cos\alpha & \chi_L\sin\alpha\sin\varphi' & \chi_{L-G}\cos\alpha & 0 & \chi_O - 2\varepsilon_L & 0 \\ 0 & \chi_L\cos\varphi' & 0 & \chi_{L-G} & 0 & \chi_O - 2\varepsilon_L \end{pmatrix} \begin{pmatrix} E_{O\sigma} \\ E_{O\pi} \\ E_{G\sigma} \\ E_{G\pi} \\ E_{L\sigma} \\ E_{L\pi} \end{pmatrix} = 0, \qquad (6)$$

where $\hat{\sigma}_O$ and $\hat{\sigma}_G$ are defined to be perpendicular to the plane defined by the vectors $\mathbf{K}_O$ and $\mathbf{K}_G$ and $\hat{\pi}$ is parallel to the OGC' plane. The polarization unit vectors follow the relations $\hat{\pi}_M \times \hat{\mathbf{K}}_M = \hat{\sigma}_M$ for $M = O$, G and L. The following inner products of $\hat{\sigma}$ and $\hat{\pi}$ have been used in

Teukolsky, Vetterling & Flannery, 1992) is used in our calculation, which will be reported in the next section.

There are twelve roots for (8), among which only six roots, whose imaginary parts are non-negative, are physically meaningful if the crystal is semi-infinite.

Therefore, within the crystal there are six modes of wave propagation with six different g values or different wave vectors K_O. If a thin overlayer is considered, all the twelve modes need to be included in the calculation. The real part g' of g determines the coordinates of the tie point on the dispersion surface for given θ_i and θ_f, while the imaginary part g'' of g yields the linear absorption coefficient, $\mu = 4\pi k g''$. To clearly reveal the geometry of the dispersion surface, we show schematically in Fig. 4 the overall picture (Fig. 4a) and a cross section (Fig. 4b) of the dispersion surface in the momentum space. In Fig. 4(a), the three Ewald spheres centered at the reciprocal-lattice points O, G and L intersect with one another. The G reflection and the L reflection occur at the tie points A and B, respectively, where the two corresponding Ewald spheres intersect with the sphere centered at the point O. In Fig. 4(b), a close up of the dispersion surface is given. The azimuthal angle $\Delta\gamma$ about the origin O, corresponding to the changing θ_i and θ_f in the rod scan, is defined as

$$\Delta\gamma = \gamma_0 - \gamma$$
$$= \arccos(h/2a) - \arccos[(a^2 + h^2 - b^2)/2ah], \quad (12)$$

where $\gamma_0 = \angle \mathrm{La}OG$, $a = \cos\theta_i/\lambda$, $b = \cos\theta_f/\lambda$ and h is the horizontal component of the momentum transfer, i.e. $h = OG$. For a z-axis diffractometer at small θ_i,

$$\Delta\gamma \simeq \arccos(\lambda h/2) - \arccos\{[(q/d)^2 + h^2]\lambda/2h\} \quad (13)$$

and, for a four-circle diffractometer (i.e. $\theta_i = \theta_f$),

$$\Delta\gamma = \arccos(\lambda h/2) - \arccos(h/\{2[1 - (q/2d)^2]^{1/2}\}), \quad (14)$$

where q and d are the normal component of the momentum transfer and the lattice spacing normal to the crystal surface. As shown in Fig. 4, the loci of the tie points of the six modes are indicated schematically as the curves on the cylindrical surface spanned by the $K_O(j)$ vectors centered at the point O, where La is the Laue point for the reciprocal-lattice points O and G. For each g, the corresponding eigenvector provides the amplitude
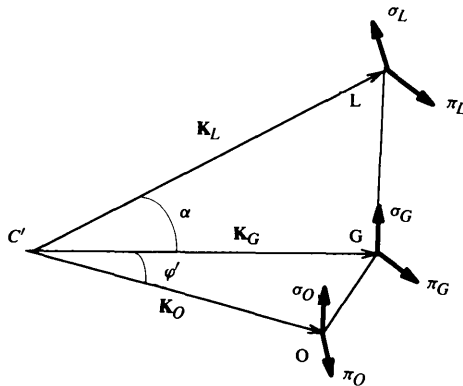

Fig. 3. Definition of the polarization unit vectors.

ratio among the wave fields E. The absolute amplitudes can be determined as usual from the following boundary conditions, i.e. the continuities of the normal components of D and B and of the tangential components of E and H at the crystal boundary ($z = 0$):

$$(e_{O\sigma} - e_{OS\sigma})\sin\theta_i = \sum_j [kg(j)/K_O(j)]E_{O\sigma}(j),$$
$$e_{O\sigma} + e_{OS\sigma} = \sum_j [K_O(j)/k]E_{O\sigma}(j),$$
$$e_{O\pi} + e_{OS\pi} = \sum_j E_{O\pi}(j), \quad (15)$$
$$(e_{O\pi} - e_{OS\pi})\sin\theta_i = \sum_j g(j)E_{O\pi}(j)$$

for the forward transmitted O waves,

$$-e_{G\sigma}\sin\theta_f = \sum_j [kg(j)/K_G(j)]E_{G\sigma}(j),$$
$$e_{G\sigma} = \sum_j [K_G(j)/k]E_{G\sigma}(j),$$
$$e_{G\pi} = \sum_j E_{G\pi}(j), \quad (16)$$
$$-e_{G\pi}\sin\theta_f = \sum_j g(j)E_{G\pi}(j)$$

for the G reflected waves, and

$$-e_{L\sigma}\sin\theta_f = \sum_j \{k[g(j) - l/k]/K_L(j)\}E_{L\sigma}(j),$$
$$e_{L\sigma} = \sum_j [K_L(j)/k]E_{L\sigma}(j),$$
$$-e_{L\pi}\sin\theta_f = \sum_j [g(j) - l/k]E_{L\pi}(j), \quad (17)$$
$$e_{L\pi} = \sum_j E_{L\pi}(j)$$

for the L reflected waves, where e and E are the wave-field amplitudes outside and inside the crystals, respectively, and $e_{OS\sigma}$ and $e_{OS\pi}$ are the σ and π components of the surface specularly reflected wave fields, respectively. For an infinitely thick crystal, the variables $e_{OS\sigma}$, $e_{OS\pi}$, $e_{G\sigma}$, $e_{G\pi}$, $e_{L\sigma}$, $e_{L\pi}$ and the six $E_{O\sigma}(j)$ with $j = 1$–6 can be determined by the 12 equations given in (15), (16) and (17).

Finally, the intensity of the rod for given θ_i and θ_f can be calculated as

$$I(\Delta\gamma) = I(\theta_i, \theta_f)$$
$$= [(|e_{G\sigma} + e_{L\sigma}|^2 + |e_{G\pi} + e_{L\pi}|^2)\sin\theta_f]$$
$$\times [(|e_{O\sigma}|^2 + |e_{O\pi}|^2)\sin\theta_i]^{-1}. \quad (18)$$

For a thin overlayer, the intensity of the rod scan can be calculated in the same way except that the 12 modes of wave propagation need to be considered and the effective surface structure factor $F(Q)$ and the phase factor $\exp(iQr)$ should be included in the structure factor F_M

of (4), where r is the relative displacement of the layer with respect to the substrate and Q is the momentum transfer. Moreover, for very accurate calculations and for the intensity distribution along the direction not lying in the OGL plane, more reciprocal-lattice points in the vicinity of the G point could be included.

By knowing the wave-field amplitudes E, the excitation $Ex(j)$ of mode j of wave propagation and the excitation Ex_M of beam M can be calculated as

$$Ex(j) = \sum_{M=O,G,L} E_M^*(j)E_M(j)/|E_O|^2(\sin\theta_f/\sin\theta_i) \quad (19a)$$

$$Ex_M = \sum_j E_M^*(j)E_M(j)/|E_O|^2(\sin\theta_f/\sin\theta_i), \quad (19b)$$

where E_M^* is the complex conjugate of E_M. The excitation of mode is equivalent to the modulus of the Poynting vector associated with mode j. From the mode excitation, linear absorption coefficients and dispersion surface, one can also calculate the X-ray penetration depth $\zeta(j)$ for each mode, as $\zeta(j) = 1/kg''(j)$, and the resultant penetration depth ζ_r can be determined as

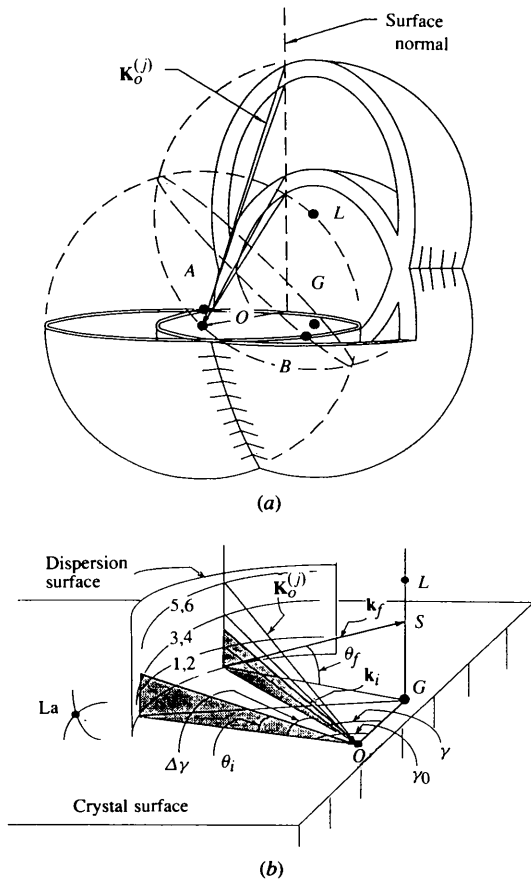$$\zeta_r = \sum_j \zeta(j)Ex(j). \quad (20)$$

(a)

(b)

Fig. 4. (a) Overall view and (b) close-up view of the dispersion surface involved in the rod scan.

Table 1. *Refined g' and g'' values*

	g'	g''
1	0.216078363	0.000034648
2	0.216149654	0.000026428
3	0.216307873	0.000008199
4	0.216379069	0.000000012
5	1.189635397	0.000017312
6	1.189635520	0.000021422

4. Numerical calculations

The theoretical consideration given in the previous section is very similar to the conventional dynamical theory for multibeam diffraction except that a numerical calculation scheme needs to be employed in order to approach asymptotically and eventually find the correct eigenvalues for (8). In this section, we will concentrate on the numerical calculation to determine the eigenvalues. For the overall dynamical calculation in general, readers are referred to the standard multibeam calculation procedures reported in the literature (*e.g.* Colella, 1974; Chang, 1984).

We use the Newton–Ralph method (Press *et al.*, 1992) to find the eigenvalues g. The difficulty encountered is that the calculated g converges to the different roots of (8) with different starting (initial) values. In other words, for given θ_i and θ_f, the final values of g depend on the initial values of g. In addition, g is complex. Therefore, we are facing a two-dimensional non-linear equation of g. To overcome the uncertainty of finding the final correct values of g, we simply calculate g for each possible initial value, the real g' and the imaginary g'', and scan over all possible points in the $g'g''$ plane to find the most probable values. For the conservation of the total energy, the allowed g values should be those with $g'' \geq 0$. Usually, the most probable values determined are still different from the correct eigenvalues and need to be refined by substituting the probable values into (8) so as to have the $|\Phi|$ value as close to zero as possible. Normally, the order of magnitude of g is the same as that of $\sin\theta_i$ or $\sin\theta_f$, namely close to unity. When the accuracy in refining g reaches the level of 10^{-11} and the value of the determinant $|\Phi|$ is very close to zero, the refined g values are considered as the correct eigenvalues for (8).

As an example, for the W(200) rod, we set the initial value as $g_i = |R|\exp(i\theta)$ in the Newton method. If g_i lies in the first or the fourth quadrants, then g tends to converge asymptotically to the roots with $g'' > 0$. If g_i lies in the second or the third quadrants, g tends to approach the roots with $g'' < 0$. For this reason, we only scan our initial g_i values over the quadrants I and IV. If we set the scan ranges for R and θ from 0 to 2 and from -90 to $90°$, respectively, then the final six refined roots at $\theta_i = \theta_f = 12.5°$ can be calculated, and these are listed in Table 1.

Why does the conventional dynamical theory fail to calculate the intensity distribution of a non-specular rod?

Table 2. *Real and imaginary parts of the structure factors* $(Cu K\alpha_1)$

Crystal	Reflection	Real part	Imaginary part
Si	000	113.9520	2.64
	111	−60.9877	−1.8667
NiSi$_2$	000	214.1280	4.6760
	111	82.6660	2.0360
W	000	135.9040	11.1540
	200	−96.8676	−11.1540
	202	80.9478	11.1540

The reason is the following: suppose we do not employ the Newton–Ralph method to find the eigenvalues in an asymptotic way, we could rather assume as an approximation that each mode has the same path length in the crystal so that g in (10) and (11) can be substituted by $\sin \theta_i$. With this approximation, (8) can be expanded as a linear equation of 12th order in g. Solving this polynominal equation is equivalent to finding the eigenvalues of the following asymmetric matrix B of rank 12 (Colella, 1974):

$$B = \begin{pmatrix} C_1 & C_0 \\ I & 0 \end{pmatrix}, \qquad (21)$$

which implies that

$$\Phi = -Ig^2 + C_1 g + C_0 = 0 \qquad (22)$$

holds, with

$$C_1 = \begin{pmatrix} 0 & 0 & 0 & 0 & 0 & 0 \\ 0 & 0 & 0 & 0 & 0 & 0 \\ 0 & 0 & 0 & 0 & 0 & 0 \\ 0 & 0 & 0 & 0 & 0 & 0 \\ 0 & 0 & 0 & 0 & 2l/k & 0 \\ 0 & 0 & 0 & 0 & 0 & 2l/k \end{pmatrix} \qquad (23)$$

where I = identity matrix and 0 = null matrix.

As is well known, the eigenvalues of such an asymmetric matrix equation cannot be accurately determined and the inaccuracy increases as the Euclidean norm (Press *et al.*, 1992) increases, where the Euclidean norm is defined as the sum of the squares of all the elements in the matrix B. As can be seen from (21) and (24), the Euclidean norm of B increases when θ_i increases. Therefore, this approximation is valid only for cases involving small θ_i. In fact, the non-specular rod scans involve a large angular range for θ_i and θ_f. This

demonstrates why the conventional dynamical theory, including the generalized approach recently reported by Stepanov (1994) and Stepanov & Köhler (1994), could not account for the intensities of the whole rod. The use of an iteration procedure could be one of the solutions to this problem.

5. Results and discussion

The dynamical calculations include the intensities of NiSi$_2$/Si (111) specular rod and W (200) non-specular rod for Cu $K\alpha_1$ radiation. The input data are the X-ray wavelength used, $\lambda = 1.540562$ Å, the structure factors, and the angles θ_i and θ_f, which are related to the momentum transfer. The structure factors used are listed in Table 2, where the imaginary parts are deduced from the data of anomalous dispersion given in *International Tables for X-ray Crystallography* (1974) and the temperature factor (at 298 K) are included.

Fig. 5(a) shows the calculated intensity distribution of the NiSi$_2$/Si (111) rod with the dynamical approach (the solid curve), the kinematical (the dashed curve) and the kinematical plus Fresnel reflectivity (the dot-dashed curve). The experimental curve indicated by squares is taken from the report by Robinson *et al.* (1988) for 25 Å thick NiSi$_2$ on Si (111), where both θ_i and θ_f are varying during the rod scan. Since this specular rod involves only the 111 reflection with no in-plane momentum transfer, (8) can be solved analytically. Owing to the sample system consisting of an overlayer NiSi$_2$, 25 Å thick, and the Si substrate, the dynamical calculation procedures presented above are employed to take care of the diffractions from both the overlayer and the substrate. The kinematical calculation is carried out by following

$$C_O = \begin{pmatrix} \chi_O + \sin^2 \theta_i & 0 & \chi_{\bar{G}} & 0 & \chi_{\bar{L}} \cos \alpha & 0 \\ 0 & \chi_O + \sin^2 \theta_i & 0 & \chi_{\bar{G}} \cos \varphi' & \chi_{\bar{L}} \sin \alpha \sin \varphi' & \chi_{\bar{L}} \cos \varphi' \\ \chi_G & 0 & \chi_O + \sin^2 \theta_f & 0 & \chi_{G-L} \cos \alpha & 0 \\ 0 & \chi_G \cos \varphi' & 0 & \chi_O + \sin^2 \theta_f & 0 & \chi_{G-L} \\ \chi_L \cos \alpha & \chi_L \sin \alpha \sin \varphi' & \chi_{L-G} \cos \alpha & 0 & \chi_O + \sin^2 \theta_f - 4(l/2h) & 0 \\ 0 & \chi_L \cos \varphi' & 0 & \chi_{L-G} & 0 & \chi_O + \sin^2 \theta_f - 4(l/2h)^2 \end{pmatrix}, \qquad (24)$$

the equation given below:

$$I(q) = C_l |F(Q)|^2 \{ [\sin^2(q_1 a_1 N_1/2) \sin^2(q_2 a_2 N_2/2)]$$
$$\times [\sin^2(q_1 a_1/2) \sin^2(q_2 a_2/2) 4 \sin^2(q a_3/2)]^{-1} \}, \qquad (25)$$

where q_1, q_2 and q are the three components of the momentum transfer Q and q is normal to the crystal surface. N_1, N_2 and N_3 are the numbers of crystal unit cells along the q_1, q_2 and q directions and a and C_l are the lattice constants and the proportional constant, respectively. $F(Q)$ is the effective surface structure factor.

As mentioned in the previous section, the kinematical theory, which does not consider the boundary conditions, cannot therefore handle refraction and reflection caused by the boundary between two media. For this reason, we add the Fresnel reflectivity to the kinematical calculated intensities for comparison. As can be seen from Fig. 5(a), the kinematical plus Fresnel reflectivity curve well simulates the dynamical curve in the region off the 111 reflection peak position, where refraction effects are dominant. Near the 111 peak, both the dynamical and kinematical curves are coincident with the measured curve. At the peak, the kinematical intensity goes to infinity. Owing to the lack of the measured peak intensity in the work of Robinson *et al.* (1988) for comparison, we then carried out the intensity measurement on a 600 Å thick $NiSi_2$ layer on the Si (111) surface with Cu $K\alpha_1$ radiation using a rotating-anode X-ray source and a five-circle diffractometer. Fig. 5(b) shows the measured and the dynamical calculated intensity distribution of the rod. The peaks A and B are due to Si and $NiSi_2$, respectively. The experimental broadening due to the horizontal beam divergence of 0.14°, the vertical angular resolution of 0.06° and the crystal mosaicity of 0.01° are convoluted with the dynamical calculated profile. Fairly good agreement between the measured and the calculated profiles is obtained. Owing to the weak scattered intensity off the peak, the statistical errors for the tails are large compared with the peak intensity.

Fig. 6 shows the intensity distributions of a non-specular rod of W (200) surface. The solid and dashed curves are the dynamical and the kinematical calculated results and the measured data (the squares) are taken from the literature (Robinson, 1986). Both θ_i and θ_f vary during the scan. Since this case involves the excitation of two reflections, 200 and 202, the dynamical calculation with the Newton–Ralph method is necessary to find the correct eigenvalues for g because the conventional dynamical theory fails to describe this non-specular rod. Since the detailed experimental conditions were not reported by Robinson, Waskiewicz, Tung & Bohr (1986), we assume in the dynamical calculation that the instrumental broadening is a Gaussian which is composed of the beam divergences and the crystal mosaic
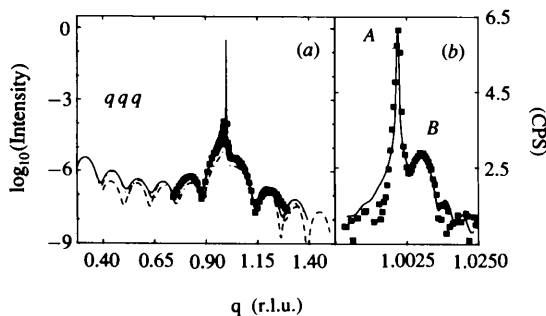

Fig. 5. Calculated and measured intensity distributions of $NiSi_2$/Si (111) rod scans: (a) 25 Å $NiSi_2$, and (b) 600 Å $NiSi_2$.

spread and the latter is also a Gaussian with half-width Λ, Λ being a function of the penetration depth ζ, *i.e.*

$$\Lambda(\zeta) = A\{(1 + \delta) - \text{erf}[(\zeta - \zeta_0)/2^{1/2}\Lambda_0]\}, \quad (26)$$

where A, δ and Λ are the limits, *i.e.* $\Lambda = \Lambda_S$ as $\zeta \to \infty$ and $\Lambda = \Lambda_F$ as $\zeta \to -\infty$, and δ and A take the values

$$\delta = 2/[\Lambda_F/\Lambda_S - 1],$$
$$A = \Lambda_S/\delta.$$

This assumption of the mosaic spread as an error function is to some extent reasonable because from (26) the width of an in-plane diffraction peak is larger than that of an off-plane peak. For convenience, we do not use the dynamical penetration depth but the kinematical one in the calculation to simplify the data analysis. The latter is defined as (Dosch, Batterman & Wack, 1986)

$$\zeta = 1/[2\pi(l_i + l_f)], \quad (27)$$

where

$$l_i = 1/2^{1/2}\{(2\Delta - \sin^2\theta_i)$$
$$+ [(\sin^2\theta_i - 2\Delta)^2 + (2\Delta')^2]^{1/2}\}^{1/2},$$
$$l_f = 1/2^{1/2}\{(2\Delta - \sin^2\theta_f)$$
$$+ [(\sin^2\theta_f - 2\Delta)^2 + (2\Delta')^2]^{1/2}\}^{1/2}.$$

The quantities Δ and Δ' are the corrections in the refractive index, *i.e.* $n = 1 - \Delta - i\Delta'$.

The convolution of the dynamical calculated profile and the instrumental broadening with $\Lambda_S = 0.15°$, $\Lambda_F = 1.2°$ and $\Lambda_O = 200$ Å gives the resultant calculated profile. In addition, in order to estimate in a simpler manner the crystal-surface roughness from this non-specular rod, we use the multiplication of the calculated profile with the roughness β, defined by Robinson (1986) as the final form for the dynamically calculated intensity profile, though a more rigorous treatment of surface roughness has been proposed (Harada, 1993). As shown in Fig. 6, the kinematical curve with $\beta = 0.46$(1), corresponding to a roughness of 1.05 Å, is less well fitted to the experimental curve than the dynamical curve with $\beta = 0.25$(1), corresponding to 1.98 Å surface roughness. Moreover, at the peak positions the kinematical calculation blows up. This fact causes a serious problem in analyzing the surface diffraction data because in the literature most surface diffraction data have been analyzed with the kinematical theory, which provides no definite scales for the peak intensity and the momentum transfer (the peak position). The appropriateness of the best-fitted kinematical curve is therefore questionable. On the contrary, the dynamical theory gives absolute scales for the intensity and the momentum transfer. Parameters, such as the surface roughness, determined from the dynamical fitting to the peak width and peak

height are in principle more reliable than those determined from the kinematical fitting.

Figs. 7 and 8 show the calculated dispersion surface, the linear absorption coefficients and the mode excitation at $\theta_i = 0.7°$ with varying θ_f for the W (200) rod (Fig. 6). Fig. 7(a) shows the six dispersion curves *versus* $\Delta\gamma$ at $\theta_i = 0.7°$. Since the curves of modes 1 and 2 are very close to each other, we therefore plot a single curve to represent the pair of the closely spaced dispersion curves. The two points A and B are the positions at which the 200 and 202 reflections take place, respectively, *i.e.* $\Delta\gamma = 0$ and 45°. The calculated intensity distribution *versus* $\Delta\gamma$ is given in Fig. 7(b). The corresponding excitations of beam Ex_M for $M = O$, G and L are shown in Fig. 7(c), where the summation is taken over all the modes. The excitation of the direct beam is always very strong because the energy flow in the O direction comes from the incident beam and decreases at $\Delta\gamma = 45°$ where the 202 reflection takes place. The G and L beams are mostly excited at the (200) and (202) positions, as expected. Fig. 7(d) shows the excitations of modes 1 and 2, namely $Ex(j)$ for $j = 1$ and 2, where the sum is over all the diffracted beams. As can be seen in this figure, mode 1 is much more strongly excited than mode 2 and the others, *i.e.* modes 3, 4, 5 and 6 (we only show here the two modes with appreciable excitation). Both the excitations of modes 1 and 2 have, respectively, a minimum and a maximum value in between the 200 and 202 positions, *i.e.* $\Delta\gamma = 30°$. Both the excitations of modes 1 and 2 exhibit a complementary feature between the two, namely, the sum of the two excitations is a constant and at $\Delta\gamma = 45°$ mode 1 is slightly peaked while mode 2 has a dip in excitation. This is due to the presence of the 202 reflection.

Fig. 8 shows the close up of the dispersion surface, the linear absorption coefficients and the mode excitations near the two positions A and B of Fig. 7(a). As shown in Fig. 8(a) near the 200 reflection, the dispersion curves exhibit the distorted hyperbola for the transmitted 200 reflection, where the distortion results from the cut of the dispersion surface normal to the crystal surface (see Fig. 4). Fig. 8(b) shows the linear absorption coefficients of the six modes. Only modes 1 and 3 contribute to the abosrption as referred to the mode excitations shown in Fig. 8(c). The asymptotic μ approaches the ordinary linear absorption value at $\theta_i = 0.7°$, $\mu_0 = 4\pi Im[k(n^2 - \cos^2\theta_i)^{1/2}] \doteq 4 \times 10^5$ cm^{-1} (where $n^2 = 1 + \chi_O$), as the position far from the 200 reflection point, *i.e.* for large $\Delta\gamma$. Figs. 8(d)–(f) show the dispersion curves, μ and $Ex(j)$ for the 202 reflection near the point B. The dispersion curve of mode 1 in Fig. 8(d) shows a resonance-like curve, which is a characteristic of a Bragg-type reflection, namely, the two branches of the hyperbola are connected by the solution curve (Chang, 1977) due to the 202 total reflection. Indeed, the linear
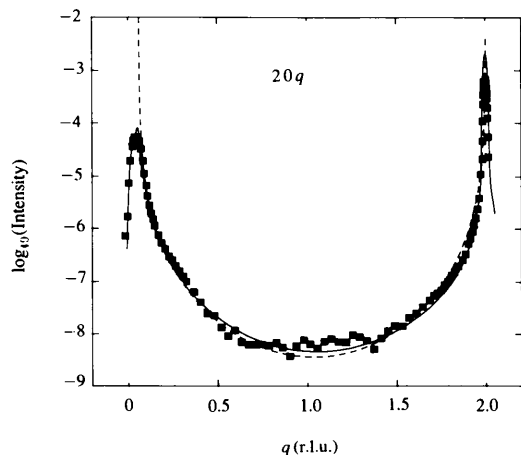

Fig. 6. Calculated and measured intensity distribution of W (200) rod scan (solid curve: dynamical calculation with 1.05 Å surface roughness; dashed curve: kinematical calculation with 1.98 Å roughness).
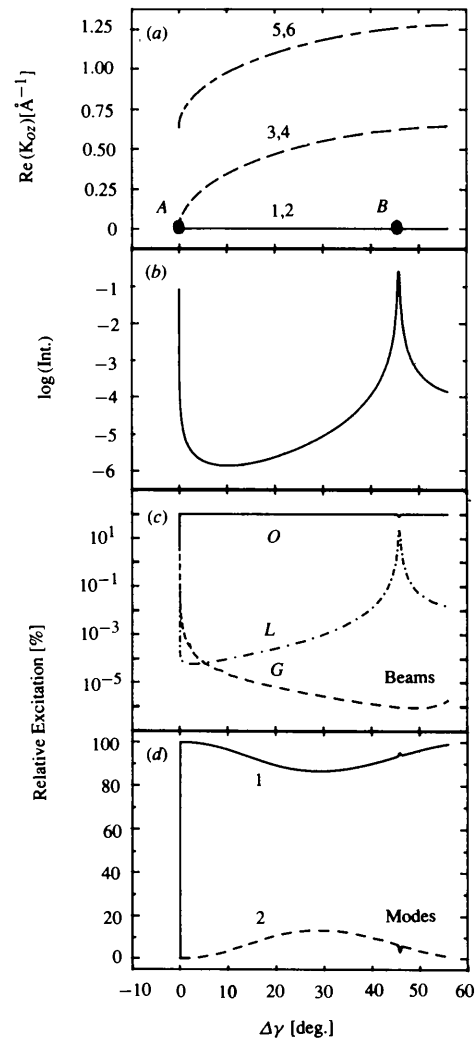

Fig. 7. Calculated dispersion curves (a), intensity distribution (b), excitation of beam (c), and excitation of mode (d) of the W (200) rod.

absorption coefficient of mode 1 is peaked in this total reflection region, as expected. The asymptotic value is also about 4×10^7 m^{-1} as $\Delta\gamma$ is far away from the 202 reflection position (Fig. 8e). Again, mode 1 is the most excited mode in the diffraction process and is peaked near $\Delta\gamma = 45°$ when the 202 reflection occurs (Fig. 8f). From these figures, we learn that the dispersion surface, the linear absorption coefficients μ and the excitation of mode Ex(j) remain their two-beam diffraction characters. Therefore, the diffraction in the rod scan is nothing more than a coalescence of a glancing Laue-type and an asymmetric Bragg-type reflection.

Since the kinematical theory cannot account for the intensities at the diffraction peak positions for surface X-ray diffractions, the dynamical approach presented here needs to be used to calculate the peak intensities. An immediate question that can be asked is: within what angular or momentum-transfer range near the peak is the use of the dynamical theory a must? According to the derivation given in Appendix B, this range is ca $k|\chi_L\chi_{\bar{L}}|/[8\sin^2\theta_L(\sin\theta_L - \sin\theta_i)]$ from the peak of the L reflection involved, where θ_L is the Bragg angle. For the W (200) case, the 202 reflection within 0.02 reciprocal-lattice units from the peak must be treated by this dynamical approach. For stronger reflection and smaller Bragg angle θ_L, this range is wider. That is, the kinematical theory is invalid in this range.

6. Concluding remarks

In conclusion, we have demonstrated in detail the dynamical calculation procedure for the intensity distributions of surface X-ray diffraction. The approach is quite general which can be applied to specular and non-specular surface rod scans for crystal surfaces and overlayers. In this paper, we have also pointed out the invalidity of the kinematical theory and the difficulties encountered by both the kinematical theory and the conventional dynamical theory in describing X-ray diffraction from surfaces and interfaces. In addition, the calculations for the dispersion surface, mode excitation and absorption give a better insight into the diffraction
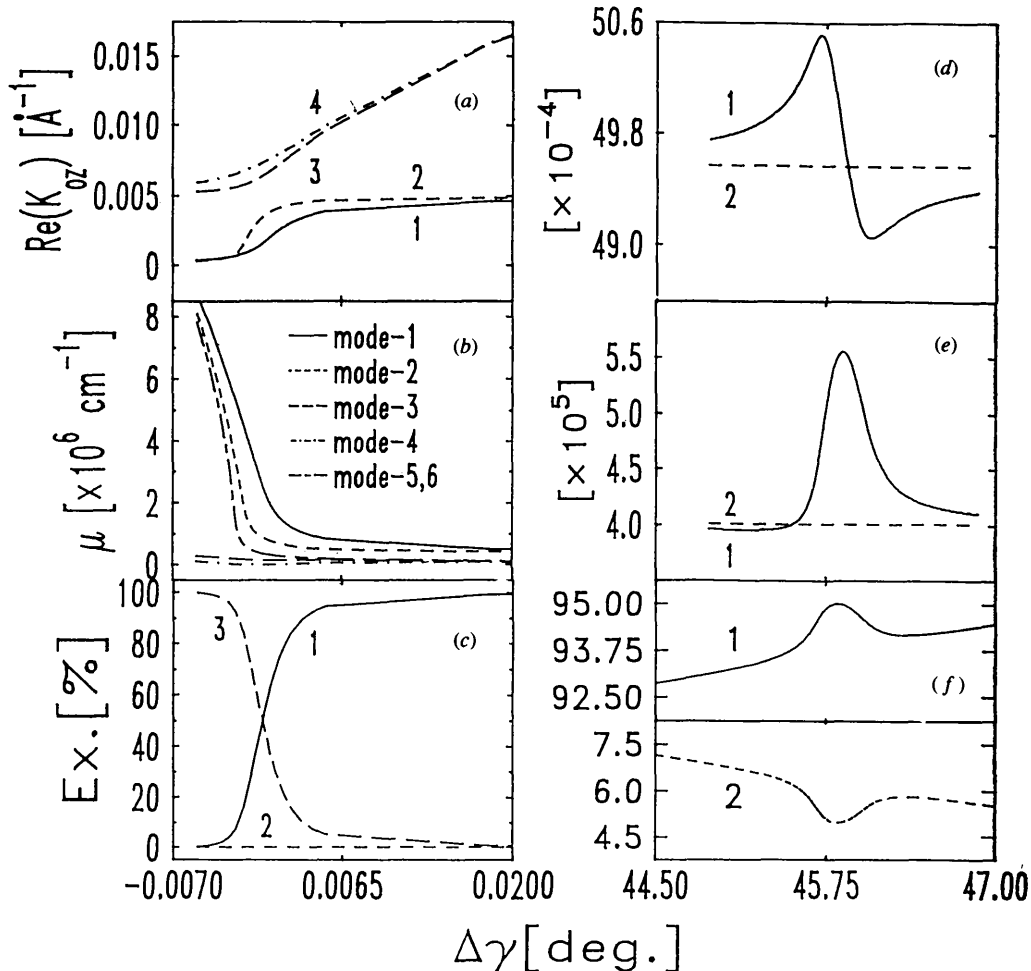

Fig. 8. Calculated dispersion curves (a), linear absorption coefficients (b) and excitation of mode (c) near the W 200 reflection and the corresponding calculated values (d), (e) and (f) near the W 202 reflection.

mechanism involved in the surface diffraction which differs considerably from the diffraction of crystal bulk. Moreover, the calculation procedure proposed provides a useful means of analyzing crystal surface roughness and penetration depth from the measured diffraction data. Through this dynamical calculation, the scale of intensity *versus* momentum transfer can be absolutely defined.

It should, however, be mentioned that in the present analysis of surface roughness we have taken an over-simplified step in the dynamical calculation. For a more rigorous approach, proper boundary conditions considering the presence of surface roughness should be derived both for the dispersion relation and the wave-field amplitudes. This is, of course, not an easy task but could in principle provide a detailed microscopic picture on diffraction from a rough surface.

APPENDIX A
Derivation of equations (10) and (11)

Referring to Fig. 9, $K_{O//}$, K_{OZ} and $K_{G//}$, $K_{GZ} = (MG)$ are the components parallel and perpendicular to the crystal surface of the wave vectors $\mathbf{K}_O$ and $\mathbf{K}_G$, respectively. With the assumption that $K_{O//}$ is along the x axis, the crystal surface normal is in the z direction and the reciprocal-lattice vector $\mathbf{OG}$ lies in the xy plane, $\mathbf{K}_O$ and $\mathbf{K}_G$ can be expressed as

$$K_O = (k\cos\theta_i, 0, -K_{OZ}), \qquad (A1)$$

$$K_G = (k\cos\theta_f\cos\varphi, k\cos\theta_f\sin\varphi, -K_{OZ}), \qquad (A2)$$

where the relations $\mathbf{K}_G = \mathbf{K}_O + \mathbf{OG}$ and $|K_{OZ}| = |K_{GZ}|$ hold. Hence, the angle φ' between $\mathbf{K}_O$ and $\mathbf{K}_G$ takes the form

$$\cos\varphi' = (\mathbf{K}_O \cdot \mathbf{K}_G)/|K_O|/|K_G|$$
$$= (k^2\cos\theta_i\cos\theta_f\cos\varphi + K_{OZ}^2)$$
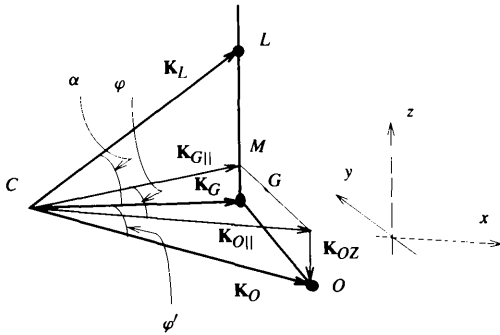$$\times \{[k^2\cos^2\theta_i + K_{OZ}^2]^{1/2}[k^2\cos^2\theta_f + K_{OZ}^2]^{1/2}\}^{-1}.$$
$$(A3)$$

Fig. 9. Geometry for the derivation of equations (10) and (11).

By substituting K_{OZ} by kg, (10) is then obtained. From Fig. 9,

$$\alpha = \angle\,LCM + \angle\,MCG$$
$$= \arctan[(l - K_{OZ})/k\cos\theta_f] + \arctan(K_{OZ}/k\cos\theta_f), \qquad (A4)$$

where $l = |GL| = |\mathbf{K}_L - \mathbf{K}_G|$. Since $\tan(a + b) = (\tan a + \tan b)/(1 - \tan a\tan b)$, $\tan\alpha$ can be written as

$$\tan\alpha = lk\cos\theta_f/[k^2\cos^2\theta_f - kg(l - kg)], \qquad (A5)$$

where the relation $K_{OZ} = kg$ has been employed. Hence, (11) is obtained.

APPENDIX B
Derivation of the angular range within which the kinematical theory is invalid

For simplicity, we consider the case involving only two reciprocal-lattice points O and L, where the reciprocal-lattice vector $\mathbf{OL}$ is perpendicular to the crystal surface. The fundamental equation for the wave field of this two-beam diffraction can be written as

$$(\chi_O + \sin^2\theta_i - g^2)E_O + \chi_L E_L = 0,$$
$$\chi_L E_O + [\chi_O + \sin^2\theta_i - (g - L/k)^2]E_L = 0, \qquad (B1)$$

where $L = |OL|$. The corresponding dispersion equation takes the following form:

$$g^4 - 2bg^3 + (b^2 - 2a)g^2 + 2abg + a^2 - ab^2 - c = 0, \qquad (B2)$$

where $a = \chi_O + \sin^2\theta_i$, $b = L/k$, and $c = \chi_L\chi_{\bar L}$. The solutions of (B2) are

$$g = (b \pm \{b^2 + 4[a \pm (ab^2 + c)^{1/2}]\}^{1/2})/2. \qquad (B3)$$

If the crystal is semi-infinitely thick and the crystal position is set far from the Bragg diffraction position, only the two solutions given below, out of the total four roots, are physically significant and are close to the kinematical form:

$$g(1) \simeq (\chi_O^2 + \sin^2\theta_i)^{1/2} = a^{1/2},$$
$$g(2) \simeq L/k + (\chi_O^2 + \sin^2\theta_i)^{1/2} = b + a^{1/2}. \qquad (B4)$$

Employing the boundary conditions

$$e_O + e_{OS} = E_O(1) + E_O(2),$$
$$e_O\sin\theta_i - e_{OS}\sin\theta_i = g(1)E_O(1) + g(2)E_O(2),$$
$$e_L = E_L(1) + E_L(2), \qquad (B5)$$
$$-e_L\sin\theta_i = \{[kg(1) - L]/k\}E_L(1)$$
$$+ \{[kg(2) - L]/k\}E_L(2),$$

and assuming that $E_O(1) = \xi(1)e_L$ and $E_O(2) = \xi(2)e_L$,

the wave-field amplitude e_L can be determined as

$$e_L = (2 \sin \theta_i) e_O / \{[g(1) + \sin \theta_i] \xi(1)$$
$$+ [g(2) + \sin \theta_i] \xi(2)\}, \qquad (B6)$$

where

$$\xi(1) \equiv (\{[g(1) - b]^2 - a\}/\chi_2)$$
$$\times \{[\Gamma(2) + \sin \theta_i]/[\Gamma(2) - \Gamma(1)]\},$$

$$\xi(2) \equiv \{\chi_L/[g^2(2) - a]\}$$
$$\times \{[\Gamma(1) + \sin \theta_i]/[\Gamma(1) - \Gamma(2)]\}$$

and

$$\Gamma(1) \equiv g(1) - b, \quad \Gamma(2) \equiv g(2) - b.$$

By substituting $g(1)$ and $g(2)$ of ($B4$) into the two terms involved in the denominator of ($B6$), we obtain

$$\xi(1)[g(1) + \sin \theta_i] \fallingdotseq (8 \sin^2 \theta_i/\chi_L)$$
$$\times [\sin \theta_L - (\chi_O + \sin^2 \theta_i)^{1/2}],$$

$$\xi(2)[g(2) + \sin \theta_i] \fallingdotseq [\chi_L(\sin^2 \theta_L - \sin^2 \theta_i)]$$
$$\times [2 \sin^2 \theta_L(\sin \theta_L + \sin \theta_i)]^{-1}.$$

Clearly,

$$\xi(1)[g(1) + \sin \theta_i] \gg \xi(2)[g(2) + \sin \theta_i]$$

and

$$e_L \simeq (2 \sin \theta_i) e_O / \{[g(1) + \sin \theta_i] \xi(1)\}. \qquad (B7)$$

From ($B1$) and ($B5$), we obtain

$$\xi(1) = \{[b^2 - 2b(a)^{1/2}]/\chi_L\}[(a^{1/2} + \sin \theta_i)/b]. \qquad (B8)$$

By substituting ($B8$) into ($B7$), e_L becomes

$$e_L \fallingdotseq [2 \sin \theta_i/(a^{1/2} + \sin \theta_i)][\chi_L/(b^2 - 2ba^{1/2})]$$
$$\times [b/(a^{1/2} + \sin \theta_i)]$$

$$\simeq 1/(4 \sin \theta_i)\{\chi_L/[\sin \theta_L - (\chi_O + \sin^2 \theta_i)^{1/2}]\}, \qquad (B9)$$

where $2 \sin \theta_L = L/k_O = b$. Equation ($B9$) is nothing more than a kinematical expression (Caticha, 1993). Therefore, up to now we have derived the kinematical expression ($B9$) from the dynamical theory. The validity of this derivation relies on whether the conditions imposed by ($B4$) hold. In other words, we can start from ($B3$) and look for the condition under which the eigenvalue g approaches the kinematical values given in ($B4$).

For simplicity, we consider only one of the solutions

$$g(1) = (b - \{b^2 + 4[a - (ab^2 + c)^{1/2}]\}^{1/2})/2. \qquad (B10)$$

If $c = 0$, then $g(1) = a^{1/2}$ and ($B4$) holds. In general, c is not equal to zero but $c = |\chi_L \chi_{\bar{L}}| \ll 1$. Hence,

$$\{b^2 + 4[a - (ab^2 + c)^{1/2}]\}^{1/2} \fallingdotseq b - 2a^{1/2} - c/[a^{1/2}b(b - 2a^{1/2})]$$

and

$$g(1) \fallingdotseq a^{1/2} + c/[2a^{1/2}b(b - 2a^{1/2})]$$
$$\equiv a^{1/2} + \Delta R. \qquad (B11)$$

Obviously, ($B11$) approaches ($B4$) if $\Delta R \ll 0$, where

$$\Delta R = (\chi_L \chi_{\bar{L}})/\{8(\chi_O + \sin^2 \theta_i)^{1/2} \sin \theta_L$$
$$\times [\sin \theta_L - (\chi_O + \sin^2 \theta_i)^{1/2}]\}$$
$$\simeq (\chi_L \chi_{\bar{L}})/[8 \sin^2 \theta_L(\sin \theta_L - \sin \theta_i)]. \qquad (B12)$$

If the momentum transfer lies in the range $k\Delta R$, with $\Delta R \neq 0$, then the kinematical theory is invalid. A similar proof can be found in Zachariasen (1967).

References

AFANES'EV, A. M. & MELKONYAN, M. K. (1983). Acta Cryst. A39, 207–210.

ANDREWS, S. R. & COWLEY, R. A. (1986). J. Phys. C, 18, 6427–6439.

CATICHA, A. (1993). Phys. Rev. B, 47, 76–83.

CATICHA, A. (1994). Phys. Rev. B, 49, 33–38.

CHANG, S. L. (1977). Phys. Status Solidi A, 47, 717–722.

CHANG, S. L. (1984). Multiple Diffraction of X-rays in Crystals. Berlin: Springer-Verlag.

COLELLA, R. (1974). Acta Cryst. A30, 413–423.

COLELLA, R. (1991). Phys. Rev. B, 34, 13827–13832.

DOSCH, H., BATTERMAN, B. W. & WACK, D. C. (1986). Phys. Rev. Lett. 56, 1144–1147.

DOSCH, H., MAILANDER, L., REICHERT, H., PEISL, J. & JOHNSON, R. L. (1991). Phys. Rev. B, 43, 13172–13186.

FEIDENHANS'L, R. (1989). Surf. Sci. Rep. 10, 105–188.

FEIDENHANS'L, R., PEDERSON, J. S., BOHR, J., NIELSEN, M., GREY, F. & JOHNSON, R. L. (1988). Phys. Rev. B, 38, 9715–9720.

GAU, T. S. & CHANG, S. L. (1994). Phys. Lett. A, 196, 223–228.

GREY, F., FEIDENHANS'L, R., NIELSEN, M. & JOHNSON, R. L. (1989). J. Phys. (Paris) Colloq. C7, 181–187.

HARADA, J. (1993). Ultramicroscopy, 52, 233–237.

HELD, G. A., JORDAN-SWEET, J. L., HORN, P. M., MAK, A. & FELDMAN, L. C. (1989). Solid State Commun. 72, 36–41.

International Tables for X-ray Crystallography (1974). Vol. III. Birmingham: Kynoch Press. (Present distributor Kluwer Academic Publishers, Dordrecht.)

JEDRECY, N., SAUVAGE-SIMKIN, M., PINCHAUX, R., MASSIES, J., GREISER, N. & ETGENS, V. H. (1990). Surf. Sci. 230, 197–204.

KASHIWAGURA, N., KAHIHARA, Y., SAKATA, M., HARADA, J., WILKINS, S. W. & STEVENSON, A. W. (1987). Jpn. J. Appl. Phys. 26, L2026–2029.

LIANG, K. S., SIROTA, E. B., D'AMICO, K. L., HUGHES, G. J. & SINHA, S. K. (1987). Phys. Rev. Lett. 59, 2447–2450.

MARRA, W. C., EISENBERGER, P. & CHO, A. Y. (1979). J. Appl. Phys. 50, 6927–6933.

MOCHRIE, S. G. J., ZEHNER, D. M., OCKO, B. M. & GIBBS, D. (1990). Phys. Rev. Lett. 64, 2925–2928.

NAKATANI, S. & TAKAHASHI, T. (1994). Surf. Sci. 311, 433–439.

PRESS, W. H., TEUKOLSKY, S. A., VETTERLING, W. T. & FLANNERY, B. P. (1992). Numerical Recipes in C. Cambridge Univ. Press.

ROBINSON, I. K. (1986). Phys. Rev. B, 33, 3830–3836.

ROBINSON, I. K., TUNG, R. T. & FEIDENHANS'L, R. (1988). Phys. Rev. B, 38, 3632–3635.

ROBINSON, I. K. & TWEET, D. J. (1992). Rep. Prog. Phys. 55, 599–651.

ROBINSON, I. K., WASKIEWICZ, W. K., FUOSS, P. H., STARK, J. B. & JOHNSON, R. L. (1986). Phys. Rev. B, 33, 7013–7016.

ROBINSON, I. K., WASKIEWICZ, W. K., TUNG, R. T. & BOHR, J. (1986). Phys. Rev. Lett. 57, 2714–2717.

SHIMURA, T. & HARADA, J. (1993). *J. Appl. Cryst.* **26**, 151–158.
STEPANOV, S. A. (1994). *Crystallogr. Rep.* **39**, 182–187.
STEPANOV, S. A. & KOHLER, R. (1994). *J. Appl. Phys.* **78**, 7809–7815.

VINEYARD, G. H. (1982). *Phys. Rev. B*, **26**, 4146–4159.
ZACHARIASEN, W. H. (1967). *Theory of X-ray Diffraction in Crystals.* New York: Dover.

Single-Crystal Data Collection with a Laue Diffractometer

BY J. LANGE AND H. BURZLAFF

Institut für Angewandte Physik, Lehrstuhl für Kristallographie der Universität Erlangen-Nürnberg, Bismarckstrasse 10, 91054 *Erlangen, Germany*

Dedicated to Professor Dr M. M. Woolfson

Abstract

The Laue technique is suitable to study effects that depend on wavelength such as absorption, anomalous dispersion or secondary extinction. The accuracy of the measured integrated intensities for X-ray structure determination is comparable with measurements of conventionally collected data. The present paper describes and discusses the results of a single-crystal data collection with a Laue diffractometer. The results obtained from the Laue data are in very good agreement with the results from conventionally collected data.

Introduction

The availability of synchrotrons as white-radiation X-ray sources of high spectral brilliance is the reason for recent developments in Laue diffraction techniques for data collection, especially in the field of protein crystallography. Several two-dimensional detector systems are in use, such as films (*e.g.* Rabinovich & Lourie, 1987), image plates (*e.g.* Miyahara, Takahashi, Amemiya, Kamiya & Satow, 1986), multiwire proportional chambers (*e.g.* Baru *et al.*, 1978), the FAST system (Bartunik & Borchert, 1989) and others (*International Tables for Crystallography*, 1992).

Since it is the primary intention in this field to increase the speed of data collection, less attention is paid to the accuracy of a single measurement. Only one attempt (Sakamaki, Hosoya & Fukamachi, 1980) has been made to incorporate the Laue technique into an ordinary four-circle-diffractometer device. The present authors reported in a series of short communications on the hardware development of devices suitable for this purpose (Lange & Burzlaff, 1991*a,b*).

It is the intention of this paper to report first results on the basis of a medium-sized inorganic structure, to compare the data with a data set collected in the classical way and to discuss the results and the technique in comparison with the work of Sakamaki *et al.*

Measurement of integrated intensities

Single-crystal X-ray diffraction with white radiation differs from the monochromatic technique in the following ways:

1. Instead of one well defined Ewald sphere with radius $R = 1/\lambda$, a continuous distribution of Ewald spheres with $R_{min} \leq R \leq R_{max}$ is present resulting in a simultaneous diffraction process for a large number of reciprocal-lattice vectors h_j. Each vector h_i selects its own Ewald sphere depending on its position in the reciprocal space.

For the simultaneous registration of the reflections, a two-dimensional detector is necessary that allows the angular localization of the diffracted beams. In addition, the wavelength distribution within the diffracted beam has to be known. Approximately 17% (Cruickshank, Helliwell & Moffat, 1987) of all diffracted beams contain a series of $n\lambda$ related to the scattering vectors $n\mathbf{h}$ of the reflection ($n = 1, 2, 3, \ldots$).

2. In contrast to the conventional monochromatic technique, a property of the crystal is utilized in another way. With the model for a real crystal composed of small mosaic blocks, the end point of the scattering vector $\mathbf{h}$ must be replaced by a small fragment of a spherical surface. Its shape is determined by the mosaic-block distribution of the crystal.

With monochromatic radiation, scan procedures must be applied to obtain the integrated intensity originating from all mosaic blocks. In the case of white-beam diffraction, all mosaic blocks are in scattering position simultaneously since a bundle of Ewald spheres (close to the 'main' Ewald sphere for the reflection corresponding to $\mathbf{h}$) is present. No scan process is necessary for the measurement of the integrated intensity provided that the detector is suitable to collect the entire diffracted beam.

It is the basic idea of this paper to make use of the second point above concerning a single reflection $\mathbf{h}$. In order to determine the wavelengths related to a